HHS Public Access

Author manuscript

Neuroimage. Author manuscript; available in PMC 2016 September 01.

Published in final edited form as:

Neuroimage. 2015 September ; 118: 494–507. doi:10.1016/j.neuroimage.2015.06.038.

In vivo mapping of human spinal cord microstructure at 300 mT/m

Tanguy Duval[1], **Jennifer A. McNab**[2], **Kawin Setsompop**[3], **Thomas Witzel**[3], **Torben Schneider**[4], **Susie Yi Huang**[3], **Boris Keil**[3], **Eric C. Klawiter**[5], **Lawrence L. Wald**[3], and **Julien Cohen-Adad**[1,6]

[1]Institute of Biomedical Engineering, Polytechnique Montreal, Montreal, QC, Canada

[2]Department of Radiology, Stanford University, Stanford, CA, United States

[3]A.A. Martinos Center for Biomedical Imaging, Massachusetts General Hospital, Harvard Medical School, Charlestown, MA, United States

[4]NMR Research Unit, Department of Neuroinflammation, Queen Square MS Centre, UCL Institute of Neurology, London, London, United Kingdom

[5]Department of Neurology, Massachusetts General Hospital, Harvard Medical School, Boston, MA, United States

[6]Functional Neuroimaging Unit, CRIUGM, Université de Montréal, Montreal, QC, Canada

Abstract

The ability to characterize white matter microstructure non-invasively has important applications for the diagnosis and follow-up of several neurological diseases. There exists a family of diffusion MRI techniques, such as AxCaliber, that provide indices of axon microstructure, such as axon diameter and density. However, to obtain accurate measurements of axons with small diameters (<5 μm), these techniques require strong gradients, i.e. an order of magnitude higher than the 40–80 mT/m currently available in clinical systems. In this study we acquired AxCaliber diffusion data at a variety of different q-values and diffusion times in the spinal cord of five healthy subjects using a 300 mT/m whole body gradient system. Acquisition and processing were optimized using state-of-the-art methods (e.g., 64-channel coil, template-based analysis). Results consistently show an average axon diameter of 4.5 +/− 1.1 μm in the spinal cord white matter. Diameters ranged from 3.0 μm (gracilis) to 5.9 μm (spinocerebellar tracts). Values were similar across laterality (left-right), but statistically different across spinal cord pathways ($p<10^{-5}$). The observed trends are similar to those observed in animal histology. This study shows, for the first time, in vivo mapping of axon diameter in the spinal cord at 300 mT/m, thus creating opportunities for applications in spinal cord diseases.

Corresponding author: Julien Cohen-Adad, Ph.D., Institute of biomedical engineering, Polytechnique Montreal, 2900 Edouard-Montpetit Bld, Montreal, QC, H3T1J4, Canada, Tel: 514-340-4711; Fax: 514-340-4611; jcohen@polymtl.ca.

Keywords

diffusion MRI; AxCaliber; axon diameter; quantification; human; spinal cord

Introduction

The spinal cord white matter is organized into bundles of myelinated and unmyelinated axons. Each bundle, or pathway, conveys ascending or descending electrical signals that are essential to ensure adequate synergy between the brain and the peripheral nervous system. Any damage to these axons can have a dramatic impact on a person's quality of life leading to motor (paralysis) and/or sensory deficits; and, in some cases, neuropathic pain (Dijkers et al., 2009). Axon damage can have various causes, such as spinal cord injury, autoimmune and neurodegenerative diseases (e.g., multiple sclerosis), cancers, and vascular diseases. Due to the highly specific roles of each spinal pathway in the regulation of the central nervous system, the prognosis of functional recovery, for a patient who has sustained an injury, strongly depends on the type of pathways damaged (Rossignol et al., 2006). Moreover, in some pathologies, specific populations of axons are preferentially targeted: multiple sclerosis affects smaller axons first (DeLuca et al., 2004), while motor-neuron diseases target larger axons (Cluskey and Ramsden, 2001). These observations motivate the development of non-invasive biomarkers of axon diameter sizes for a better understanding of the pathophysiology of those diseases, and to improve precision of diagnosis and validation of therapeutic strategies.

In the human spinal cord, the internal diameter of myelinated axons varies from 1 to 10μm (Peters et al., 1991; Waxman et al., 1995). Large axons are believed to have higher firing frequencies and conduction velocities, at the expense of more energy used (Perge et al., 2012). Histological studies reported large differences of axonal microstructure (e.g., mean axon diameter, density and myelin membrane thickness) across spinal pathways (Dula et al., 2010; Nieuwenhuys et al., 2007). For instance, dorsal column axons in the gracilis are generally smaller than that in the cuneatus (Nieuwenhuys et al., 2007). However, due to the need for sub-micrometric resolution and the difficulty in performing histology across the entire spinal cord with large throughput, there is poor documentation of spinal cord microstructure in humans.

Diffusion magnetic resonance imaging (MRI) measures the random microscopic motion (diffusion) of water protons (Le Bihan et al., 1986; Stejskal and Tanner, 1965). In white matter, water molecules diffuse preferentially along the coherently oriented myelinated axons (Beaulieu and Allen, 1994). This anisotropic diffusion is often modeled as a tensor (diffusion tensor imaging, DTI) (Basser and Pierpaoli, 1996) and was shown to correlate with demyelination and/or axonal loss (Klawiter et al., 2011; Song et al., 2005). However, the interpretation of water diffusion via a tensor is often challenging, as diffusion anisotropy can be affected by axon density, size and shape and other fibrous structure such as scar tissue (Schwartz et al., 2005; Wheeler-Kingshott and Cercignani, 2009). A family of advanced diffusion MRI, called q-space imaging, measures the full diffusion propagation profile of water molecules at a given diffusion time (Callaghan et al., 1988), providing

metrics related to the microstructure (Lätt et al., 2008; Ong et al., 2008). Moreover, by introducing models of white matter, diffusion MRI can quantify the relative size of compartments where diffusion is restricted (within axons), hindered (between axons) and free (Gaussian) (Assaf and Basser, 2005). Based on these compartments, Assaf et al. introduced a method called "AxCaliber" which is sensitive to axon diameter distribution (Assaf et al., 2008). In practice, this is achieved by varying the strength of the diffusion-sensitizing gradients (G_{max}) and the duration between the applications of these two diffusion gradients (diffusion time, Δ). In recent years, several diffusion MRI experiments were performed in the animal ex vivo spinal cord showing (i) good contrast of microstructure parameters between the spinal cord pathways (Ong and Wehrli 2010; Shemesh et al. 2013) and (ii) better sensitivity to traumatic lesions compared to anatomical images (Nossin-Manor et al. 2002). Results from diffusion MRI in the in vivo human spinal cord also showed that metrics related to tissue microstructure could be extracted (Grussu et al. 2015).

However, model-free (Lätt et al., 2008; Ong et al., 2008) and model-based (Assaf et al., 2008) quantitative diffusion MRI methods require strong magnetic gradients (several hundreds of mT/m) in order to obtain accurate measures of axon diameters and are therefore not feasible in clinical scanners (40–80 mT/m) (Bar-Shir et al., 2008). Other model-based diffusion MRI techniques like ActiveAx (Alexander, 2008) can yield robust estimate of axon diameters even at 60 mT/m (Alexander et al., 2010; Schneider et al., 2012) but come at the expense of adding more constraints to the model, which can introduce further bias in the estimation (Alexander et al., 2010). Furthermore, despite advances in the modeling approaches to axon diameter measurements there is an intrinsic limitation in the minimum axon diameters that can be disentangled (Huang et al., 2015; Nilsson and Alexander, 2012). For example, the minimal axon diameter is around 6μm at 60mT/m and 3μm at 300mT/m (Nilsson and Alexander, 2012). This justifies the use of strong gradients for advanced diffusion MRI experiments. A corollary advantage of using stronger gradients is the possibility to achieve lower echo times (TE) while keeping b-value constant, which offers significantly higher signal-to-noise ratio (Cohen-Adad et al., 2011). Recently, the first human scanner equipped with 300 mT/m gradients showed encouraging applications in humans including mapping axon diameter distributions in the in vivo human corpus callosum (McNab et al. 2013; Huang et al. 2015).

The goals of the current study were (i) to design an experimental setup and acquire q-space AxCaliber data in the *in vivo* human cervical spinal cord using 300 mT/m gradients and (ii) to estimate axon diameters and density within specific spinal pathways. Data acquisition and processing were optimized using state-of-the-art methods, including a 64-channel coil (Keil et al., 2013) and a newly-developed template and atlas of spinal cord (Benhamou et al., 2014; Fonov et al., 2014) for automatic and unbiased quantification of metrics within specific spinal pathways.

Method

1. Acquisition

Five healthy subjects were recruited (mean age 28 +/− 11, three males). This study was approved by the institutional review board at Massachusetts General Hospital (MGH) and

written informed consent was obtained from all subjects. MR experiments were performed on a 3T system (MAGNETOM, Siemens Healthcare, Germany), equipped with a Connectom Gradient (AS302) (Setsompop et al., 2013) capable of up to 300 mT/m along each axis and a maximum slew rate of 200 mT/m/ms (downgraded to 90 mT/m/ms for the diffusion gradients due to safety concerns). A custom-made 60-channel phased-array head/neck receive coil was used, in combination with the 4 more superior elements of the commercial spine matrix (Keil et al., 2013), yielding 64 channels. The isocenter was set at the level of the mouth.

Diffusion weighted (DW) data were acquired using a single shot spin echo EPI sequence with monopolar gradient scheme. Four axial slices (5 mm thick) were centered at C1, C2, C3 and C4 vertebral bodies to minimize B0 inhomogeneity (Cohen-Adad et al., 2011), as illustrated in Figure 1. Optimal shim coefficients of second order were calculated within a small box encompassing the spinal cord (green box in Figure 1). Two saturation bands were prescribed anterior and posterior to the spinal cord to prevent aliasing in the phase-encoding direction (A-P) (red grids in figure 1).

Q-space was sampled in the plane orthogonal to the slice-select gradient (i.e., orthogonal to the main direction of spinal tracts) along four opposite directions: XY, -XY, X-Y and -X-Y, as illustrated in Figure 2.a. These four directions were chosen in order to (i) correct eddy-current distortions using the reversed-gradient method (Bodammer et al., 2004), (ii) minimize the bias introduced by fibers that would be not perfectly aligned along Z and (iii) maximize gradient strength by a factor √2, given that 300 mT/m is available in each channel and can be summed up. Sampling density was increased quadratically towards high q-values to overcome the loss of SNR and be more sensitive to smaller axon diameters.

Sequence parameters were: pulse width δ= 8 ms, maximal gradient strength G_{max} = √2 * 300 = 410 mT/m, diffusion times Δ = {20, 35, 50} ms, TE = {65, 70, 85} ms (minimized for each diffusion time), TR ≈ 2 s (depends on cardiac rate), voxel size = 0.8×0.8×5 mm^3, matrix size = 128×128, bandwidth = 1185 Hz/pixel, R=2 acceleration with GRAPPA reconstruction, effective echo spacing (accounting for acceleration) = 0.49 ms. Acquisitions were cardiac-gated using pulse oximeter probe. Acquisition window for gating was set to 700 ms and started at 100 ms after the pulse oximeter peak to be in the quiescent regime (Summers et al., 2006). Acquisition time for the AxCaliber protocol was around 30 min for a total of 623 images.

In addition to the AxCaliber protocol, 43 volumes were acquired with diffusion gradients rotating about the spinal cord axis (see Figure 2.b), with b-value set to 8,770 s/mm^2 (δ=8 ms, Δ =50 ms, G_{max}=200 mT/m). This was done to quantify the contribution of axons that were not perfectly aligned along the Z axis, as they would create an angular dependence on the diffusion-weighted signal.

2. Preprocessing

Eddy-current correction—Reversed-gradients technique was used for correcting eddy-current artifacts (Bodammer et al., 2004). This technique consists of estimating the transformation between two images acquired with opposite diffusion gradient directions. To

improve accuracy, each slice was corrected independently, assuming only rigid transformation (Tx, Ty). No scaling or shearing was estimated, which, to our preliminary data, was a satisfactory assumption, given that the spinal cord occupies a relatively small region (~1×1 cm^2), and hence is minimally affected by transformations that scales with X and Y. The slice-wise correction was preferred to the volume-based correction because the amplitude of eddy-current artifacts varied along Z, yielding non-rigid deformations. Transformations were estimated with FSL FLIRT (Jenkinson et al., 2002), using a custom-made schedule file[1]. A 2D Gaussian mask centered on the spinal cord was used as a weighting mask in order to register the spinal cord independently from the rest of the body (e.g., surrounding muscles, fat). All transformations were then saved (for final combination with motion correction transformations) and applied (for estimating motion correction, see below).

Motion Correction—After correcting for eddy-current distortions, subject motion was estimated on a slice-by-slice basis using the same schedule file as before (Tx, Ty) and the same Gaussian mask. Contrary to previous studies (Cohen-Adad et al., 2008), interspersed b=0 images were not used to estimate subject motion, because CSF flow affected some b=0 images differently and hence could have introduced spurious motion correction parameters. Instead, motion was estimated based on the diffusion-weighted images that ranged between b-values of 430 s/mm^2 and b-values of 4000 s/mm^2. These values were empirically chosen so that images presented sufficient SNR and no visible CSF contamination (see Figure 3). The first image was used as the reference image for registration (i.e., target image).

To further improve the robustness of the motion correction, x-translations and y-translations were respectively approximated by a spline function (see Figure 4). This approach was chosen empirically, under the assumption that subject motion is slow with time (low frequency drifts). Images acquired at b<430 and b>4000 s/mm^2 were corrected using extrapolated transformation values from the spline function.

As a final step, in order to reduce the number of interpolations, transformation matrices from eddy-current and motion corrections were combined and applied only once using sinc interpolation.

Normalization of DW data related to variable TE—All DW data were divided by the mean b=0 image of the corresponding TE to account for T2 relaxation. Here we assumed a single T2 compartment for normalization (see discussion about potential presence of multiple T2 compartments). An additional normalization step was set for each group of Δ during curve fitting (see model fitting below).

Bias correction and noise reduction—Magnitude data were bias-corrected assuming Rician noise using the method of (Gudbjartsson and Patz, 1995):

$$A = \sqrt{|M^2 - \sigma^2|} \quad (1)$$

[1]https://github.com/neuropoly/spinalcordtoolbox/blob/master/flirtsch/schedule_TxTy.sch

Where A is the true voxel intensity, M is the measured voxel intensity and σ is the standard deviation of the Gaussian noise. The parameter σ was computed by calculating the standard deviation within a moving window (size = 15) along q-values, after detrending the data using the AxCaliber model. All the calculated standard deviations were then averaged within the spinal cord. Preliminary results showed similar sigma across the three Δ values, therefore the three calculated sigma were averaged. Noise was then reduced using the Local Principal Component Analysis (LPCA) algorithm using (Manjón et al., 2013). The reader is referred to the discussion for the potential impact of the LCPA filter for axon diameter estimation.

3. Model fitting

A modification of the AxCaliber model was implemented in Matlab (MathWorks, Natick, MA). The model was assumed to have two compartments (restricted and hindered) but only a single axon diameter, as proposed in the ActiveAx technique (Alexander et al., 2010). Throughout this manuscript we refer to the AxCaliber model for clarity. Also, fibers were assumed to be oriented along Z.

The model was fitted using a non-linear least square algorithm (using trust-model-reflective optimization), with a maximum of ten iterations for fast convergence (we empirically found that more iterations did not improve accuracy of fitting). Six parameters were estimated: fraction hindered (fh), diffusion hindered coefficient (Dh), mean diameter (d), and the intensities I_{b0}(TE=65 ms), I_{b0}(TE=70 ms) and I_{b0}(TE=85 ms). These parameters are related by the following equation: $I = I_{b0}(\Delta)[fh.Eh.(Dh) + (1-fh).Er(d)]$, where Eh and Er are the signal decay in the hindered and restricted compartment respectively and are defined as follow (Callaghan, 1995):

$$Eh = exp\,(-bD_h) \quad (2)$$

$$E_r = \sum_{k=0}^{\infty}\left[4\exp\left(-\frac{4\beta_{0k}{}^2 D_r \Delta}{d^2}\right)\times\left[\frac{\pi qd \times J_0'(\pi qd)}{(\pi qd)^2 - \beta_{0k}{}^2}\right]^2 + \sum_{n=1}^{\infty} 8\exp\left(-\frac{4\beta_{nk}{}^2 D_r \Delta}{d^2}\right)\times\frac{\beta_{nk}{}^2}{\beta_{nk}{}^2 - n^2}\times\left[\frac{\pi qd \times J_n'(\pi qd)}{(\pi qd)^2 - \beta_{nk}{}^2}\right]^2\right] \quad (3)$$

Where J_n' is the first derivative of the n[th] Bessel function of the first kind and β_{nk} its k[th] zero crossing. Dr represents the diffusion coefficient in the restricted compartment. See discussions concerning the violation of small pulse approximation.

The fraction of restricted compartment was deduced by complementarity: fr = 1 − fh. Diffusion coefficient for the restricted compartment (Dr) was set to 1.4 μm^2/ms (Barazany et al., 2009). No cerebrospinal fluid (CSF) compartment was included in the model (see Discussion).

The fitting procedure was run voxel-by-voxel using broad limits: fh [0 1]; Dh [0 3] μm2/ms; d [1 10] μm; [0 2]. Results were plotted and visually inspected. The quality of the fit was assessed by computing the reduced chi-squared statistic for each voxel.

4. Post-processing

Registration to template—Data from all subjects were registered to the white matter template available from the MNI-Poly-AMU template (Fonov et al., 2014). The transformation was estimated from an average of high b-value DW images (>3000 s/mm^2), as these images exhibited the best white/gray matter contrast. A diffeomorphic transformation was estimated using the SyN method available in ANTs (Avants et al., 2008) (see Figure 5).

Extraction of metrics within spinal pathways using maximum likelihood—An atlas of spinal pathways (Benhamou et al., 2014) was used to extract model-based diffusion MRI metrics within specific tracts (see Figure 5d). Briefly, the atlas was constructed from an existing anatomical reference (Standring, 2008) and then merged within the MNI-Poly-AMU template. The atlas consists of 30 different pathways, each of them accounting for partial volume effect (values ranging from 0 to 1). In order to disentangle voxels overlapping with adjacent pathways, model-based diffusion MRI metrics were estimated using the maximum likelihood estimation described in the following equation, which assumes homogeneous metric value within each tract:

$$M_{voxel_i} = \sum_{tracts} p_{voxel_i, tract_j} M_{tract_j} \quad (4)$$

Where M_{voxel_i} is the observed metric at voxel i, and M_{tract_j} is the metric to estimate for tract j(assuming homogeneous tracts). $p_{voxel_i, tract_j}$ is the volume fraction of tract j in voxel i, given by the atlas.

If we define the matrix $P = (p_{voxel_i, tract_j})_{i,j}$, we can recast the problem in the form:

$$\overrightarrow{M_{voxels}} = P\overrightarrow{M_{tracts}} \quad (5)$$

Then, the vector $\overrightarrow{M_{tracts}}$ is calculated by computing the pseudoinverse of matrix P:

$$\overrightarrow{M_{tracts}} = (P^t P)^{-1} P^t \overrightarrow{M_{voxel}} \quad (6)$$

All scripts used for preprocessing, template registration and metrics extraction are freely available in the Spinal Cord Toolbox (http://sourceforge.net/projects/spinalcordtoolbox/).

Statistics—SNR was computed voxel-wise by dividing average values (extracted from fits) by the σ computed previously (see section: “Bias correction and noise reduction”).

The reduced chi-squared statistic of the fitting curves was calculated voxel-by-voxel as follows:

$$\chi^2_{red} = \frac{\chi^2}{v} = \frac{1}{v} \sum \frac{(O - E)^2}{\sigma^2} \quad (7)$$

where O are the observed data, E are the theoretical data (i.e. from the AxCaliber model), is the Gaussian noise standard deviation and $\mathscr{V}$ is the degree of freedom, given by $N-n-1$, where N is the number of observations, and n is the number of fitted parameters. Here, N=623 and n=6. Based on previous studies validating the AxCaliber model (Panagiotaki et al. 2012), we anticipate χ^2_{red} values to be close to one.

The quantity $\chi^2=\chi^2_{red}\cdot v$ follows a chi-squared distribution f using the degree of freedom ν. To assess whether the AxCaliber model correctly fitted our data, the area under the χ^2 distribution (α) was calculated as follows:

$$\alpha=\int_{\chi^2_{vox}}^{\infty} f(x)\,dx \quad (8)$$

Due to the large degree of freedom ν, a significant difference between the fitted model and the data is expected to be found, resulting in very small values of α.

A three-way ANOVA was performed to assess whether there are any significant differences (significance level set to p=0.05) of axon diameters between the pathways of each subject, between the right and the left pathways, and between the five subjects themselves.

Reproducibility tests—The reproducibility of extracted metrics over the direction of diffusion gradients was assessed by analyzing two sub-datasets of acquired q-space data (see figure 13): one with diffusion-gradient along (−X,+Y; +X, −Y) and one along (−X, −Y; +X, +Y). Each sub-dataset was processed separately and then compared.

The reproducibility of extracted metrics over q-space sampling was assessed using a bootstrap analysis in one subject. Q-space data were randomly subsampled by 10% and 90% were kept for analysis. This procedure was run 200 times in order to derive standard deviations, related to q-space sampling, of extracted metrics in each voxel.

Orientation dependence—The rotational symmetry of water diffusion in the spinal cord was studied using the data from the protocol b (figure 2.b). After normalizing with the b=0 images, the curve representing the MR signal as a function of gradient direction was low-pass filtered using sine and cosine functions. The peak-to-peak variation was used to indicate the orientation dependence. The angle at the minima (i.e., larger signal loss) corresponded to the direction of the crossing fibers.

Results

1. Quality of the data

Data were successfully acquired in all five subjects. Figure 6 illustrates data acquired in a subject at four different b-values (0, 450, 5924 and 39011 s/mm2). Even at maximum b-value (39,011 s/mm^2, with δ=8 ms, Δ=50 ms and G=300*√2=424 mT/m), signal from the spinal cord white matter is visible. The majority of this signal likely comes from the restricted compartment, given that the signal from the hindered and free compartments was lost due to the strong dephasing.

Figure 7 shows the data in one subject averaged across q, before and after applying eddy-current and motion correction. The corrected data shows sharper edges, suggesting that the preprocessing pipeline was effective. Notice the visible gray/white matter contrast, which was helpful in registering the spinal cord to the template while maintaining consistent anatomical topology during mapping spinal pathways from the template.

Figure 8 shows the q-space data in one representative voxel in the white matter in one subject. There is a clear separation of q-space data across the three groups of Δ suggesting that the model adequately identified the hindered versus the restricted compartments. Notice that the data acquired with small diffusion time (Δ=20ms, blue) exhibit stronger signal with monotonic decay, due to the residual signal in the hindered compartment. Data acquired with large diffusion time (Δ=50ms, red) plateau for q-space values above 0.08 μm^{-1}, suggesting that the signal mostly originates from the restricted compartment given the near-complete attenuation of the hindered compartment. Assuming a diffusion coefficient Dh>0.5 μm^2/ms, the attenuation is over 98% at q>0.08 μm^{-1} (see Eq.2).

2. SNR analysis

Figure 9 shows the standard deviation across q, calculated using a moving window (size = 15) after detrending the data with AxCaliber fits. In all subjects, the standard deviation ranged from 8% to 15% of the b=0 signal.

SNR (static + temporal) was computed voxel-wise by dividing average values (extracted from fits) by noise standard deviation. Table 1 shows SNR results per vertebral level in all subjects. SNR averaged across vertebral levels ranged between 1.4–2.0 in the b_{max}=39,011 s/mm^2 images and 9.0–11.7 in the b=0 images for all subjects. In two subjects, SNR was higher at C4 level, which could be attributed to (i) closer proximity of this region to the neck coil in these two subjects and/or (ii) lower amplitude of cardiac-related noise, as it was shown that this amplitude varies across subjects and vertebral levels (Piché et al., 2009).

3. Quality of q-space Fitting

Table 2 shows the average χ^2_{red} for all subjects. Each value is the average of the χ^2 across voxels within the spinal cord. Here, values range between 1.09 and 1.23, suggesting a good fit. Supplementary material S1 shows the reduced chi-squared statistics of AxCaliber fitting in one subject. Values for α associated with the χ^2_{red} statistics were less than 5% (except for subject 3), meaning that the model did not fit the data appropriately (See discussion). Supplementary material S2 shows two q-space fitting in two different voxels, yielding in two different quality of fit (α=0.13 and α=9E-9).

Figure 10 shows AxCaliber fitting in one subject in three different ROIs. The fitted curves exhibit different shapes between the three regions, which is expected because the underlying microstructure (axon size and density) is different across the three regions. Conversely, when comparing neighboring voxels within a given region however, the fitted curves exhibit a similar shape (not shown here). These observations suggest that the AxCaliber model is reproducible and sensitive to differences in microstructures.

4. Mapping of axon diameter

The first two columns of Figure 11 exhibit maps of the estimated hindered water volume fraction (fh) and the apparent diffusion coefficient of the hindered compartment (Dh). These maps were registered to the template and averaged across subjects (N=5). Since the model did not account for CSF compartment (in order to achieve higher precision), any partial voluming with CSF at the periphery of the cord translated into a more elevated Dh. The two last columns show the mean and standard deviations of axon diameters. Here, the single axon diameter model was used (Alexander et al., 2010). Results are consistent across slices and across subjects, as assessed by the relatively low standard deviation maps. Axon diameters ranged from 3.0μm in the gracilis at C4 to 5.9μm in the spinocerebellar tract at C2. In the posterior funiculus (black arrow), estimated axon diameters get smaller towards the inferior direction.

Figure 12 reports numerical values of mean axon diameter, fh and Dh per subject, within specific pathways. The restricted water fraction (1−fh), which correlates with axon density (Alexander, 2008), was the highest in the cuneatus and the lowest in spinothalamic tract with 55% and 44% of intra-axonal water, respectively. Standard deviation of axon density across subjects was remarkably low (<0.02), suggesting good reproducibility of the technique and stability of this parameter across individuals. Mean axon diameters (across subjects and across vertebral levels) ranged from 3.51 μm (+/− 0.54) in the gracilis to 4.15 μm (+/− 0.46) in the cuneatus tract. In each subject taken individually, axon diameter and density were smaller in the gracilis than in the cuneatus. The same trends were reported in literature regarding the human spinal cord (Trobe, 2010). Dh was somewhat uniform (0.65 +/− 0.12 $\mu m^2/ms$) within the whole white matter. A three-way ANOVA tested the dependence towards laterality (left/right), pathways (five pathways were included in the ANOVA) and subjects. Results show an effect of pathway ($p<10^{-5}$) and subject ($p<10^{-7}$), but no effect for laterality (p=0.24). The interaction terms were not significant, i.e., Laterality*Subject (p=0.19), Laterality*Pathway (p=0.07) and Subject*Pathway (p=0.73). Supplementary material S3 shows axonal diameter histograms for each subject, computed in the entire white matter.

5. Orientation dependence and reproducibility

Effect of gradient direction—The resulting mean difference between the two sub-datasets (within the white matter, across subjects and vertebral levels) was 1.1μm for axon diameter and 0.08 for hindered water fraction (fh). Figure 13 (right panel) shows the resulting map of axon diameter difference between the two sub-datasets in one subject. Other subjects showed similar trends. Large differences between exp #1 and exp #2 are observed in the lateral and dorsal regions, and can be attributed to the presence of collateral fibers, as previously shown in monkeys (Lundell et al., 2011). The presence of collateral fibers violates the assumption of fibers being solely oriented along the spinal cord axis (as was assumed here), inducing orientation-dependence when applying diffusion gradients perpendicular to the spinal cord axis.

Orientation dependence—The change in signal amplitude as a function of gradient orientation was 22 % (averaged in the white matter across subjects), confirming the presence

of an orientation dependence. Figure 14c. shows the principal direction of the collateral fibers computed from the highest diffusion peak. Notice that in the lateral portion of the spinal cord, collateral fibers have orthogonal directions between the left and the right side and are oriented diagonally, which corroborate the observations from Figure 13. Figure 14d. shows a map of orientation dependence obtained from the peak-to-peak amplitude in the orientation dependence plot (averaged across subjects and located at C2). Higher angular dependence was found in dorsal roots regions at C1 and C2. This was expected, as this region encompasses longitudinal fibers as well as transverse, as shown in *ex vivo* monkey spinal cord with PAS-MRI (Lundell et al., 2011).

Bootstrap analysis—The average standard deviations of the fitting parameters were found to be 0.25μm for axon diameter and 0.02 for hindered water fraction (fh) in the white matter (95 percentile of the voxels).

Discussion

The purpose of this study was to demonstrate mapping of axon diameter in the *in vivo* human spinal cord using model-based q-space diffusion MRI at 300 mT/m. Model-estimated diameters fall within the range of those reported from previous histology work, opening the door to *in vivo* evaluation of specific features of spinal cord axons. The following discussion covers aspects related to the acquisition and preprocessing, diffusion model fitting (including discussions about noise) interpretation of axon diameter maps and future work.

1. Interpretation of axon diameter maps

Validation against histology—There is very little literature on axon diameter mapping in the human spinal cord. Histological data reporting quantitative values of axon diameters were found only for the pyramidal tracts. In this tract, 89.6% of axons were reported to range from 1 to 4μm, 8.7% from 5 to 10 μm, and 1.7% from 11 to 20 μm (Lassek, 1945). When accounting for the larger signal contribution from larger axons (Alexander et al. 2010), the volume-weighted average axon diameter is 7.82 μm. This value is larger than that from the corticospinal found in the present study (4.14 μm), which can be partly explained by the violation of the small pulse approximation. When using Gaussian Phase Distribution (GDP) approximation, the average axon diameter is 6.05μm (supplementary material S4). However, some discrepancies remain, which can come from a combination of fibre dispersion (not modelled), permeability of unmyelinated axons (not modelled), and other oversimplifications of the model, as well as skewed sensitivity to large axons. Figure 15 compares AxCaliber results with two histological resources: optical micrographs and maps of cytoarchitecture obtained from adult individuals with no records of neurological diseases (Nieuwenhuys et al., 2007). Trends were similar between histology and AxCaliber results: large axons in the spinocerebellar tract (4–5 μm), moderate axons in the rubrospinal tract (3–4 μm) and small axons in the gracilis (2–3 μm). In the posterior funiculus (black arrow in Figure 11), estimated axon diameters get smaller towards the inferior direction. This observation is in accordance with previous histology work (Nieuwenhuys et al., 2007). Notice that the gracilis, composed of small axons, has larger surface at C4 than at C1 levels due to incoming fibers from the cuneatus. Also notice the heterogeneity of axon diameter

within tracts (as seen on the optical micrographs), suggesting that single-axon models are not appropriate. Future studies of histological validation in *ex vivo* human spinal cord are needed.

When comparing our results with those from studies on animals, the same trends are observed between tracts. For example, results in the gracilis, cuneatus and rubrospinal tracts (3.51, 4.14, 3.92 μm respectively) show the same trends in rats (1.1, 2.7, 1.1 μm) (Chin et al., 2004) and mice (0.99, 1.40, 1.16 μm) (Ong and Wehrli, 2010).

Inter-subject variability—Results showed rather large inter-subject variability, relative to the within-subject inter-tract variability (see Figure 12). However it is worth mentioning that the maps of axon diameter were consistent across subjects, i.e., gracilis smaller than the cuneatus, or corticospinal smaller than spinothalamic. Causes for the inter-subject variability can be anatomical and/or artifactual. Artifactual causes are related to noise (i.e., different noise levels owing to variable coil loading, inducing bias in the estimation) and to the variable subject motion. The hypothesis of a noise-related bias is supported by a strong correlation ($r=0.94$, $p=0.02$) between axon diameter (Figure 15) and SNR (Table 1), although this will have to be confirmed in a larger population. It is also possible that the fiber composition could vary between subjects, which could in turn induce bias in the estimation of axon diameters. Also, we cannot rule out the possibility of the curvature of the cord varying across subjects, which would result in a variable degree of orthogonality between the spinal cord centerline and the imaging slices. However, if present, this effect is presumed to be minimal given the relatively small longitudinal coverage (C1–C4) as well as the careful positioning of each subject performed to reduce cervical lordosis.

Tract by tract analysis—Microstructure was assumed to be homogeneous (i.e., single diameter) within each tract of the spinal cord atlas used for metrics extraction. Despite the advantages of atlas-based analysis for objectivity (free from user-bias) and accuracy (accounts for partial volume effect using Gaussian mixture model), there are limitations. Firstly, the transition between two neighboring tracts might be progressive, resulting in non-homogeneous microstructure around the interface. For example, the rubrospinal and corticospinal tracts are partially overlapped (Altman and Bayer, 2001). Secondly, the classical delimitation of tracts is not based on microstructure but on macroscopic observations. For example, the cuneatus is separated from the gracilis by a septum (Standring et al., 2005). However, this pathway is a combination of thin fibers emerging from the sixth thoracic level and of thick fibers coming from the eighth cervical level (Carpenter, 1976; Nieuwenhuys et al., 2007). Thirdly, the delimitation of tracts in the present study was based on an atlas, which assumed the same spatial parcellation across individuals. However, the human spinal cord morphology was reported to vary across individuals (Kameyama et al., 1995). Fourthly, microstructure is not necessarily homogeneous along the spinal cord (e.g. the posterior funiculus as shown in Figure 11) and hence averaging microstructural features across slices might introduce further variability. Fifthly we assumed a linear relation between the axon diameter measured in a voxel and the combination of several axon diameters from each tract in that voxel. The potential biases

associated with this approach (e.g. the measured axon diameters are weighted by the density and volume of axons within each tract) requires further investigations.

2. Acquisition and preprocessing

Eddy-currents—The switching of large gradient amplitude during diffusion encoding generated large eddy-currents, which manifested as translation, scaling and shearing in the phase-encoding direction (set to A–P). Although a twice-refocusing pulse sequence (Reese et al., 2003) could have been used to minimize this effect, these sequences are also subject to longer TE, thereby decreasing the SNR. Instead, an image-based eddy-current distortion correction was implemented, as proposed in (Bodammer et al., 2004). Here, given that the spinal cord was centered in the middle of the FOV (isocenter), no scaling or shearing was apparent. Hence the correction only addressed translations along the phase-encoding direction, leading to a more robust correction. Results indeed showed satisfactory eddy-current correction (see Figure 7).

Effect of TR—Due to gating, the TR varied with the cardiac rate, which had some consequences in the signal time series. In this study, two slices were acquired per cardiac pulse, resulting in a TR of approximately 2 s. Moreover, TR was forced to be always greater than 1.6 s. The use of relatively short TR might have resulted in lower SNR due to only partial recovery of the spins given that the T1 in the spinal cord is about 800 ms at 3T (Smith et al. 2008). However, considering the SNR efficiency (i.e., SNR per unit time), the optimal TR was reported to be around 1 s at 3T in the white matter (Johansen-Berg and Behrens 2013). However, a drawback of cardiac gating with low TR is the introduction of additional variance in the diffusion time-series related to the variation of the heart rate throughout the acquisition, and therefore a variation in the recovery of the longitudinal magnetization. The impact of this additional variance for fitting diffusion models needs to be further investigated.

Different TE across Δ—The TE was minimized at each diffusion time in order to increase the SNR. To compensate for signal variation due to T2 relaxation, data were normalized using b=0 volumes, assuming the same T2 relaxation within the intra- and the extra-axonal water compartments. Although the assumption of a similar T2 in the intra- and extra-axonal compartment has been challenged (Does et al. 1998; Beaulieu et al. 1998; Whittall et al. 1997), a review by (Nilsson et al., 2013) reported that most in vivo studies have observed two components with short (10–50 ms) and long (70–130 ms) T2 relaxation times, that were respectively assigned to myelin water and to the combined intra- and extracellular water (Whittall et al. 1997; Laule et al. 2007; Deoni et al. 2008). Moreover, diffusion MRI studies based on fast- and slow diffusion components reported no dependence of the measured T2 as a function of diffusion encoding (Mulkern et al. 2000; Pfeuffer et al. 1999) (except at ultra-high field (Kunz et al. 2013)), and no detectable dependence of diffusion metrics on the TE (Huisman et al. 2006; Clark and Le Bihan 2000), again suggesting minimal T2 difference between the intra- and the extra-axonal compartments.

Effect of smoothing—The model fitting was done after eddy-current and motion correction. As a consequence, images were interpolated, which introduced spatial

correlations between neighboring voxels. If neighboring voxels belonged to a different microstructure, this could have introduced further partial volume effect across tracts of different underlying microstructures and hence less accuracy in the model. To minimize this effect, all transformations (eddy-current and motion correction) were concatenated into a single transformation in order to apply the sinc interpolation only once. Also note that the interpolation yielded an underestimation of the noise (σ) and hence a wrong correction of the magnitude bias. Nearest neighbor interpolation can overcome the alteration of the noise property, however this type of interpolation also yields inaccuracies in the motion correction and is therefore not recommended.

Noise—Even though the calculated SNR in b=0 (SNR=10.1) and b_{max}=39,011 (SNR=1.7) were low compared to previously published studies, where typical SNR in b=0 was ~20 (Bammer and Fazekas, 2003; Kim et al., 2010; Klawiter et al., 2011), it should be stressed that our calculation of SNR included both static (thermal) and temporal SNR. Static SNR could not accurately be calculated from the images using the standard background method (Koay et al., 2009) due to (i) the absence of 'pure' background caused by the use of reduced FOV, (ii) the presence of spatially-correlated noise related to GRAPPA reconstruction, and (iii) the use of a multi-channel coil (Dietrich et al., 2007). Hence, we reported the combination of both static and temporal SNR, which represents a more complete assessment of the data. Furthermore, physiological noise, which is known to be particularly significant in the spinal cord (Piché et al., 2009), was likely the dominant cause of the low SNR herein observed. While higher number of averaging (instead of higher number of q-values) would have yielded similar results than the one presented here, the rationale for sampling more densely was to qualitatively assess the goodness of fit to the chosen model. In particular, having a dense sampling towards high q-values enabled us to better assess the contribution of the Rician noise at low SNR regimes.Magnitude MR images were reconstructed from multiple channels (here 64). This procedure transforms the Gaussian distribution of complex noise in a non-symmetric and positively-defined distribution, inducing an upward bias in the magnitude signal. While signal from a single coil can be modeled with a Rician distribution, the distribution of noise from multi-channel coil using adaptive combine algorithm (Walsh et al., 2000) presents a non-central chi distribution (Aja-Fernández et al., 2011). Moreover, the GRAPPA reconstruction introduces a non-uniformity of noise distribution throughout the volume (Aja-Fernández et al., 2011). Correcting the magnitude bias requires an exhaustive characterization of noise distribution for a specific coil and reconstruction method, which was beyond the scope of this study. Here we used a Rician noise correction, which is a particular case of the non-central chi noise. It is important to notice that magnitude bias can have particularly detrimental effect on the estimation of axon diameters using AxCaliber methods, because this residual signal would increase the apparent signal from restricted water at high q-values.

LPCA correction was used for reducing the noise on the data and might have had an impact on the estimation of AxCaliber parameters. To address this issue, AxCaliber was re-run on the data without applying the LCPA filter. The resulting coefficient of variation (diameter_withLCPA vs. diameter_withoutLCPA) in each voxel in one subject ranged from

−7% to 4% at 95 percentile (mean −2%), suggesting minimal impact of the LCPA filter for estimating axon diameter.

3. Diffusion model

Small pulse approximation—In this study we used the small pulse approximation, which assumes no moving particles during the application of each diffusion gradient. Although the ratio Δ/ δ was kept larger than 2.5 (as suggested by (Bar-Shir et al., 2008)), here we used comparatively long pulses (=8 ms) in contrast to the typical AxCaliber pulse length (δ~4 ms) (Assaf et al., 2008; Barazany et al., 2009). Despite the maximum gradient switching rate of 200 mT/m/ms, we had to set the limit to 90 mT/m/ms for safety purpose. This yielded a ramp-up time of about 3.3 ms to reach 300 mT/m. Assuming a Gaussian diffusion of D_r = 1.4μm^2/ms (Barazany et al., 2009) in the intra-axonal compartment, during the application of the diffusion gradient the particles moved by an averaged distance of $l = \sqrt{4 * D_r * \delta} = 6.7\ \mu\mathrm{m}$, which is on the order of axon diameters. The violation of the small pulse approximation might have resulted in underestimation of fiber diameters (Bar-Shir et al., 2008).

However, the choice of using a relatively large δ was motivated by the possibility to achieve higher q, increasing the diffusion encoding resolution and providing higher sensitivity to smaller axon diameters (Alexander et al., 2010; Dyrby et al., 2012). The Gaussian phase approximation (Stepišnik, 1993; Wang et al., 1995) was shown to correct this bias, but the sensitivity to small axons would still be affected. We have conducted a comparison between small pulse approximation and Gaussian phase approximation (see Supplementary Material S4). As expected, results show a global increase of axon diameter of 1.6μm (averaged across subjects) in the white matter and a more stable estimation of the fraction of hindered water. Notice however that δ = 7 ms was shown to be appropriate for measuring axon diameter in the corpus callosum of monkeys (Alexander et al., 2010).

Considerations of gradient strength and axon resolution—By adding more constraints on the estimated parameters, other model-based quantitative diffusion MRI techniques like ActiveAx (Alexander et al., 2010) can yield accurate estimate of axon parameters, even at 60 mT/m (Nilsson and Alexander, 2012; Zhang et al., 2011), although axons smaller than 5 μm cannot be distinguished with this range of gradient strength (Alexander et al., 2010). The resolution limit at 300 mT/m is estimated to be slightly less than 3 μm using the minimal model of white matter based on simulations (Nilsson and Alexander, 2012). We performed a comparison of AxCaliber results with a maximal gradient strength of 80 mT/m versus 300 mT/m (Supplementary Materials S5 and S6). Results showed that the estimation of axon diameter is globally increased and that the contrast of axon diameter between pathways is lost (p=0.78). The fraction of hindered water is reduced but show similar trends between pathways, suggesting the reliability of this parameter on clinical systems.

Free water compartment—In this study we chose to remove the free water compartment. This compartment was originally proposed by Barazany (2009) to compensate for partial volume effect with the CSF. The decision to not use the free water compartment

was driven by preliminary data comparing AxCaliber results with and without an additional free water compartment (see Supplementary Material S7). These results showed that more than 10% of the free water compartment was wrongly estimated within the spinal cord, i.e., in regions not affected by partial volume with the CSF. These wrong estimations of the free water compartment size introduced larger instabilities when estimating axon diameter. On the other hand, when the free water compartment was not included, the diffusion hindered coefficient correctly compensated for the increase of free water fraction in voxels at the periphery of the spinal cord, with an estimated value of up to 3 $\mu m^2/ms$, and was thus a satisfactory replacement of the free water compartment. From the maps of axon diameter, one could notice a ring of large estimated axon diameter at the periphery. Although this estimate could partly be due to CSF contamination, it is also possible that the observed result is genuine, as previous histological studies of axon diameters in the spinal cord did report significantly larger axon diameter at the periphery of the cord (Nieuwenhuys et al., 2007). Moreover, the ring is also present in the maps when accounting for the free water compartment (see S7).

Diffusion coefficients—The model used in this study (composite hindered and restricted compartments) assumes (i) a fixed diffusion coefficient of $Dr=1.4\mu m^2/ms$ in the restricted compartment and (ii) a Gaussian apparent diffusion coefficient Dh in the hindered compartment.

In order to validate the first assumption ($Dr=1.4\mu m^2/ms$), we compared AxCaliber results using two extreme fixed diffusion coefficients: $Dr=0.3\mu m^2/ms$ and $Dr=2\mu m^2/ms$. The error on axon diameter estimation was below 1.3μm (99 percentile) and 0.1μm in average in all subjects. Also, the error on the fraction of restricted water was below 0.06 (99 percentile) and 0.006 in average in all subjects. Those results were expected since the water in the restricted compartment presents a permanent regime at the diffusion time Δ, pulse width δ, and axon diameters used in this study (model simulation not shown).

The second assumption (Gaussian apparent diffusion coefficient Dh) is not rigorously correct due to the time-dependence of the parameter Dh (Huang et al. 2015; Burcaw et al. 2015). This assumption might have biased our measurements, yielding over-estimation of axon diameter (Burcaw et al. 2015). However it should be mentioned that the use of very high b-value in this study (bmax=39,011 s/mm2) discriminated the signal from the hindered compartment, thus minimizing this effect. Note that the extracellular water is also affected by the size of the axons that hinder its diffusion.

Quality of q-space data fitting—The goodness-of-fit analysis suggested that the model used in this study did not describe the data within an acceptable level of significance ($\alpha<5\%$). However, it should be mentioned that this goodness-of-fit analysis strongly depends on the degree of freedom. Here, the degree of freedom was very large ($\nu=616$), imposing a χ^2_{red} thresholds close to 1 (1.09 for), which is difficult to achieve while maintaining a robust fit. Indeed, the simplicity of the AxCaliber model (6 parameters in our implementation) provides reproducible fitting results at the expense of accuracy. As illustrated in supplementary material S2, two voxels within the white matter can yield different qualities of fits. Poor fitting at high q-values could be caused by several factors.

First, the applied Rician correction might be too simplistic and a noise floor (magnitude bias) might be present. This hypothesis is supported by studies showing that GRAPPA reconstruction introduces higher spatially-variable magnitude bias (Aja-Fernández et al., 2011). Second, the presence of crossing fibers in the spinal cord (Cohen-Adad et al., 2008; Lundell et al., 2011) can violate the cylindrical assumption, because the attenuation of the signal would then be larger at high Δ if collateral fibers are present (i.e., orthogonal to longitudinal fibers). Third, a difference in T2 decay between the restricted and the hindered compartment would introduce a bias related to a different baseline signal (b=0) across Δ, given that the TE was different across Δ. This choice was made to minimize the TE for each Δ in order to maximize the SNR. Finally the non-negligible permeability of axon membranes might have introduced exchanges between the hindered and the restricted compartments, yielding biases when estimating the fraction in each of the compartments. This effect might be exacerbated in vivo, due to the presence of intra/extra-axonal flow triggered by active channels at the membrane surface related to the saltatory conduction of action potentials (Nilsson et al., 2013).

4. Applications and future work

Being able to non-invasively quantify axon diameter and density opens the door to understanding the pathophysiology of diseases targeting specific population of axons, such as multiple sclerosis and amyotrophic lateral sclerosis. The proposed method can therefore be used to improve the precision of the diagnosis and to validate therapeutic strategies. Amongst other possible applications is the combination of axon diameter and density with myelin density estimated from quantitative magnetization transfer (Sled and Pike, 2000) and/or macromolecular tissue volume methods (Mezer et al., 2013). Combining these quantities would enable in vivo estimation of the myelin g-ratio (Campbell et al., 2014; Stikov et al., 2011). The g-ratio is the ratio of the inner to the outer diameter of an axon. It was shown to be related to axon conduction (Pajevic and Basser, 2013) and can therefore provide a sensitive measure of pathology.

Conclusion

This paper reported *in vivo* mapping of axon diameter and density in the human spinal cord using 300 mT/m gradients. Results show similar trends with previous histology in humans and animals. Some potential biases (crossing fibers and noise) were identified and require further investigations. This method has the potential to provide relevant markers of spinal cord microstructure for diseases affecting specific fiber populations.

Supplementary Material

Refer to Web version on PubMed Central for supplementary material.

Bibliography

Aja-Fernández S, Tristán-Vega A, Hoge WS. Statistical noise analysis in GRAPPA using a parametrized noncentral Chi approximation model. Magn Reson Med. 2011; 65:1195–1206. [PubMed: 21413083]

Alexander DC. A general framework for experiment design in diffusion MRI and its application in measuring direct tissue-microstructure features. Magn Reson Med. 2008; 60:439–448. [PubMed: 18666109]

Alexander DC, Hubbard PL, Hall MG, Moore EA, Ptito M, Parker GJM, Dyrby TB. Orientationally invariant indices of axon diameter and density from diffusion MRI. Neuroimage. 2010; 52:1374–1389. [PubMed: 20580932]

Altman, J.; Bayer, SA. Development of the Human Spinal Cord: An Interpretation Based on Experimental Studies in Animals. Oxford University Press; 2001.

Assaf Y, Basser PJ. Composite hindered and restricted model of diffusion (CHARMED) MR imaging of the human brain. Neuroimage. 2005; 27:48–58. [PubMed: 15979342]

Assaf Y, Blumenfeld-Katzir T, Yovel Y, Basser PJ. AxCaliber: a method for measuring axon diameter distribution from diffusion MRI. Magn Reson Med. 2008; 59:1347–1354. [PubMed: 18506799]

Avants BB, Epstein CL, Grossman M, Gee JC. Symmetric diffeomorphic image registration with cross-correlation: evaluating automated labeling of elderly and neurodegenerative brain. Med Image Anal. 2008; 12:26–41. [PubMed: 17659998]

Bammer R, Fazekas F. Diffusion imaging of the human spinal cord and the vertebral column. Top Magn Reson Imaging. 2003; 14:461–476. [PubMed: 14872166]

Bar-Shir A, Avram L, Ozarslan E, Basser PJ, Cohen Y. The effect of the diffusion time and pulse gradient duration ratio on the diffraction pattern and the structural information estimated from q-space diffusion MR: experiments and simulations. J Magn Reson. 2008; 194:230–236. [PubMed: 18667345]

Barazany D, Basser PJ, Assaf Y. In vivo measurement of axon diameter distribution in the corpus callosum of rat brain. Brain. 2009; 132:1210–1220. [PubMed: 19403788]

Basser PJ, Pierpaoli C. Microstructural and physiological features of tissues elucidated by quantitative-diffusion-tensor MRI. J Magn Reson B. 1996; 111:209–219. [PubMed: 8661285]

Beaulieu C, Allen PS. Determinants of anisotropic water diffusion in nerves. Magn Reson Med. 1994; 31:394–400. [PubMed: 8208115]

Beaulieu C, Fenrich FR, Allen PS. Multicomponent water proton transverse relaxation and T2-discriminated water diffusion in myelinated and nonmyelinated nerve. Magn Reson Imaging. 1998; 16:1201–1210. [PubMed: 9858277]

Benhamou M, Fonov V, Taso M, Le Troter A, Sdika M, Collins L, Callot V, Cohen-Adad J. Atlas of white-matter tracts in the human spinal cord. Proceedings of the 22th Annual Meeting of ISMRM. 2014:13.

Bodammer N, Kaufmann J, Kanowski M, Tempelmann C. Eddy current correction in diffusion-weighted imaging using pairs of images acquired with opposite diffusion gradient polarity. Magn Reson Med. 2004; 51:188–193. [PubMed: 14705060]

Burcaw LM, Fieremans E, Novikov DS. Mesoscopic structure of neuronal tracts from time-dependent diffusion. Neuroimage. 2015

Callaghan PT. Pulsed-Gradient Spin-Echo NMR for Planar, Cylindrical, and Spherical Pores under Conditions of Wall Relaxation. J Magn Reson A. 1995; 113:53–59.

Callaghan PT, Eccles CD, Xia Y. NMR microscopy of dynamic displacements: k-space and q-space imaging. J Phys E. 1988; 21:820.

Campbell JSW, Stikov N, Dougherty RF, Bruce Pike G. Combined NODDI and qMT for full-brain g-ratio mapping with complex subvoxel microstructure. Proceedings of the 22th Annual Meeting of ISMRM, Milan. 2014

Carpenter MB. Human neuroanatomy, Williams and Wilkins Company, Baltimore, Maryland. 1976

Chin C-L, Wehrli FW, Fan Y, Hwang SN, Schwartz ED, Nissanov J, Hackney DB. Assessment of axonal fiber tract architecture in excised rat spinal cord by localized NMR q-space imaging: simulations and experimental studies. Magn Reson Med. 2004; 52:733–740. [PubMed: 15389948]

Clark CA, Le Bihan D. Water diffusion compartmentation and anisotropy at high b values in the human brain. Magn Reson Med. 2000; 44:852–859. [PubMed: 11108621]

Cluskey S, Ramsden DB. Mechanisms of neurodegeneration in amyotrophic lateral sclerosis. Mol Pathol. 2001; 54:386–392. [PubMed: 11724913]

Cohen-Adad J, Descoteaux M, Rossignol S, Hoge RD, Deriche R, Benali H. Detection of multiple pathways in the spinal cord using q-ball imaging. Neuroimage. 2008; 42:739–749. [PubMed: 18562214]

Cohen-Adad J, El Mendili M-M, Lehéricy S, Pradat P-F, Blancho S, Rossignol S, Benali H. Demyelination and degeneration in the injured human spinal cord detected with diffusion and magnetization transfer MRI. Neuroimage. 2011; 55:1024–1033. [PubMed: 21232610]

DeLuca GC, Ebers GC, Esiri MM. Axonal loss in multiple sclerosis: a pathological survey of the corticospinal and sensory tracts. Brain. 2004; 127:1009–1018. [PubMed: 15047586]

Deoni SCL, Rutt BK, Arun T, Pierpaoli C, Jones DK. Gleaning multicomponent T1 and T2 information from steady-state imaging data. Magn Reson Med. 2008; 60:1372–1387. [PubMed: 19025904]

Dietrich O, Raya JG, Reeder SB, Reiser MF, Schoenberg SO. Measurement of signal-to-noise ratios in MR images: Influence of multichannel coils, parallel imaging, and reconstruction filters. J Magn Reson Imaging. 2007; 26:375–385. [PubMed: 17622966]

Dijkers M, Bryce T, Zanca J. Prevalence of chronic pain after traumatic spinal cord injury: a systematic review. J Rehabil Res Dev. 2009; 46:13–29. [PubMed: 19533517]

Does MD, Beaulieu C, Allen PS, Snyder RE. Multi-component T1 relaxation and magnetisation transfer in peripheral nerve. Magn Reson Imaging. 1998; 16:1033–1041. [PubMed: 9839987]

Dula AN, Gochberg DF, Valentine HL, Valentine WM, Does MD. Multiexponential T2, magnetization transfer, and quantitative histology in white matter tracts of rat spinal cord. Magn Reson Med. 2010; 63:902–909. [PubMed: 20373391]

Dyrby TB, Søgaard LV, Hall MG, Ptito M, Alexander DC. Contrast and stability of the axon diameter index from microstructure imaging with diffusion MRI. Magn Reson Med. 2012; 70:711–721. [PubMed: 23023798]

Fonov VS, Le Troter A, Taso M, De Leener B, Lévêque G, Benhamou M, Sdika M, Benali H, Pradat PF, Collins DL, Callot V, Cohen-Adad J. Framework for integrated MRI average of the spinal cord white and gray matter: The MNI-Poly-AMU template. Neuroimage. 2014; 102P2:817–827. [PubMed: 25204864]

Grussu F, Schneider T, Zhang H, Alexander DC, Wheeler-Kingshott CAM. Neurite orientation dispersion and density imaging of the healthy cervical spinal cord in vivo. Neuroimage. 2015; 111:590–601. [PubMed: 25652391]

Gudbjartsson H, Patz S. The Rician distribution of noisy MRI data. Magn Reson Med. 1995; 34:910–914. [PubMed: 8598820]

Histology at the University of Michigan [WWW Document]. n.d. URL http://histology.med.umich.edu/medical/central-nervous-system (accessed 8.24.14).

Huang SY, Nummenmaa A, Witzel T, Duval T, Cohen-Adad J, Wald LL, McNab JA. The impact of gradient strength on in vivo diffusion MRI estimates of axon diameter. Neuroimage. 2015; 106:464–472. [PubMed: 25498429]

Huisman TAGM, Loenneker T, Barta G, Bellemann ME, Hennig J, Fischer JE, Il'yasov KA. Quantitative diffusion tensor MR imaging of the brain: field strength related variance of apparent diffusion coefficient (ADC) and fractional anisotropy (FA) scalars. Eur Radiol. 2006; 16:1651–1658. [PubMed: 16532356]

Jenkinson M, Bannister P, Brady M, Smith S. Improved optimization for the robust and accurate linear registration and motion correction of brain images. Neuroimage. 2002; 17:825–841. [PubMed: 12377157]

Johansen-Berg H, Behrens TEJ. Diffusion MRI: From Quantitative Measurement to In vivo Neuroanatomy. Elsevier Science. 2013

Kameyama T, Hashizume Y, Ando T, Takahashi A, Yanagi T, Mizuno J. Spinal cord morphology and pathology in ossification of the posterior longitudinal ligament. Brain. 1995; 118(Pt 1):263–278. [PubMed: 7895010]

Keil B, Cohen-Adad J, Porter DA, Biber S, Heberlein K. Simultaneous diffusion-weighted MRI of brain and cervical spinal cord using a 64-channel head-neck array coil at 3T. Proceedings of the 21th Annual Meeting of ISMRM. 2013:1210.

Kim TH, Zollinger L, Shi XF, Kim SE, Rose J, Patel AA, Jeong EK. Quantification of diffusivities of the human cervical spinal cord using a 2D single-shot interleaved multisection inner volume diffusion-weighted echo-planar imaging technique. AJNR Am J Neuroradiol. 2010; 31:682–687. [PubMed: 20019109]

Klawiter EC, Schmidt RE, Trinkaus K, Liang H-F, Budde MD, Naismith RT, Song S-K, Cross AH, Benzinger TL. Radial diffusivity predicts demyelination in ex vivo multiple sclerosis spinal cords. Neuroimage. 2011; 55:1454–1460. [PubMed: 21238597]

Koay CG, Ozarslan E, Pierpaoli C. Probabilistic Identification and Estimation of Noise (PIESNO): a self-consistent approach and its applications in MRI. J Magn Reson. 2009; 199:94–103. [PubMed: 19346143]

Kunz N, Sizonenko SV, Hüppi PS, Gruetter R, van de Looij Y. Investigation of field and diffusion time dependence of the diffusion-weighted signal at ultrahigh magnetic fields. NMR Biomed. 2013; 26:1251–1257. [PubMed: 23533088]

Laule C, Vavasour IM, Kolind SH, Li DKB, Traboulsee TL, Moore GRW, MacKay AL. Magnetic resonance imaging of myelin. Neurotherapeutics. 2007; 4:460–484. [PubMed: 17599712]

Le Bihan D, Breton E, Lallemand D, Grenier P, Cabanis E, Laval-Jeantet M. MR imaging of intravoxel incoherent motions: application to diffusion and perfusion in neurologic disorders. Radiology. 1986; 161:401–407. [PubMed: 3763909]

Lundell H, Nielsen JB, Ptito M, Dyrby TB. Distribution of collateral fibers in the monkey cervical spinal cord detected with diffusion-weighted magnetic resonance imaging. Neuroimage. 2011; 56:923–929. [PubMed: 21352926]

Lätt J, Nilsson M, Wirestam R, Johansson E, Larsson E-M, Stahlberg F, Brockstedt S. In vivo visualization of displacement-distribution-derived parameters in q-space imaging. Magn Reson Imaging. 2008; 26:77–87. [PubMed: 17582719]

Manjón JV, Coupé P, Concha L, Buades A, Collins DL, Robles M. Diffusion Weighted Image Denoising Using Overcomplete Local PCA. PLoS One. 2013; 8:e73021. [PubMed: 24019889]

McNab JA, Edlow BL, Witzel T, Huang SY, Bhat H, Heberlein K, Feiweier T, Liu K, Keil B, Cohen-Adad J, Tisdall MD, Folkerth RD, Kinney HC, Wald LL. The Human Connectome Project and beyond: Initial applications of 300 mT/m gradients. Neuroimage. 2013; 80:234–245. [PubMed: 23711537]

Mezer A, Yeatman JD, Stikov N, Kay KN, Cho NJ, Dougherty RF, Perry ML, Parvizi J, Le H H, Butts-Pauly K, Wandell BA. Quantifying the local tissue volume and composition in individual brains with magnetic resonance imaging. Nat Med. 2013; 19:1667–1672. [PubMed: 24185694]

Mulkern RV, Zengingonul HP, Robertson RL, Bogner P, Zou KH, Gudbjartsson H, Guttmann CR, Holtzman D, Kyriakos W, Jolesz FA, Maier SE. Multi-component apparent diffusion coefficients in human brain: relationship to spin-lattice relaxation. Magn Reson Med. 2000; 44:292–300. [PubMed: 10918329]

Nieuwenhuys R, Voogd J, van Huijzen C. The Human Central Nervous System: A Synopsis and Atlas. Springer. 2007

Nilsson M, Alexander D. Investigating tissue microstructure using diffusion MRI: How does the resolution limit of the axon diameter relate to the maximal gradient strength? Proceedings of the 20th Annual Meeting of ISMRM. 2012:3567.

Nilsson M, van Westen D, Ståhlberg F, Sundgren PC, Lätt J. The role of tissue microstructure and water exchange in biophysical modelling of diffusion in white matter. Magn Reson Mater Phys Biol Med. 2013; 26:345–370.

Nossin-Manor R, Duvdevani R, Cohen Y. q-Space high b value diffusion MRI of hemi-crush in rat spinal cord: evidence for spontaneous regeneration. Magn Reson Imaging. 2002; 20:231–241. [PubMed: 12117605]

Ong HH, Wehrli FW. Quantifying axon diameter and intra-cellular volume fraction in excised mouse spinal cord with q-space imaging. Neuroimage. 2010; 51:1360–1366. [PubMed: 20350604]

Ong HH, Wright AC, Wehrli SL, Souza A, Schwartz ED, Hwang SN, Wehrli FW. Indirect measurement of regional axon diameter in excised mouse spinal cord with q-space imaging: simulation and experimental studies. Neuroimage. 2008; 40:1619–1632. [PubMed: 18342541]

Pajevic S, Basser PJ. An optimum principle predicts the distribution of axon diameters in normal white matter. PLoS One. 2013; 8:e54095. [PubMed: 23382870]

Panagiotaki E, Schneider T, Siow B, Hall MG, Lythgoe MF, Alexander DC. Compartment models of the diffusion MR signal in brain white matter: a taxonomy and comparison. Neuroimage. 2012; 59:2241–2254. [PubMed: 22001791]

Perge JA, Niven JE, Mugnaini E, Balasubramanian V, Sterling P. Why do axons differ in caliber? J Neurosci. 2012; 32:626–638. [PubMed: 22238098]

Peters, A.; Palay, SL.; Webster, HF. The fine structure of the nervous system: neurons and their supporting cells. Oxford University Press; 1991.

Pfeuffer J, Provencher SW, Gruetter R. Water diffusion in rat brain in vivo as detected at very large b values is multicompartmental. MAGMA. 1999; 8:98–108. [PubMed: 10456372]

Piché M, Cohen-Adad J, Nejad MK, Perlbarg V, Xie G, Beaudoin G, Benali H, Rainville P. Characterization of cardiac-related noise in fMRI of the cervical spinal cord. Magn Reson Imaging. 2009; 27:300–310. [PubMed: 18801632]

Reese TG, Heid O, Weisskoff RM. Reduction of eddy-current-induced distortion in diffusion MRI using a twice-refocused spin echo. Magn Reson Insights. 2003

Rossignol S, Dubuc R, Gossard JP. Dynamic sensorimotor interactions in locomotion. Physiol Rev. 2006; 86:89–154. [PubMed: 16371596]

Schneider T, Wheeler-Kingshott CAM, Alexander DC. MAPPING THE AXON DIAMETER INDEX IN THE CORPUS CALLOSUM IS CLINICALLY FEASIBLE. Proceedings of the 20th Annual Meeting of ISMRM. 2012:350.

Schwartz ED, Duda J, Shumsky JS, Cooper ET, Gee J. Spinal cord diffusion tensor imaging and fiber tracking can identify white matter tract disruption and glial scar orientation following lateral funiculotomy. J Neurotrauma. 2005; 22:1388–1398. [PubMed: 16379577]

Setsompop K, Kimmlingen R, Eberlein E, Witzel T, Cohen-Adad J, McNab JA, Keil B, Tisdall MD, Hoecht P, Dietz P, Cauley SF, Tountcheva V, Matschl V, Lenz VH, Heberlein K, Potthast A, Thein H, Van Horn J, Toga A, Schmitt F, Lehne D, Rosen BR, Wedeen V, Wald LL. Pushing the limits of in vivo diffusion MRI for the Human Connectome Project. Neuroimage. 2013; 80:220–233. [PubMed: 23707579]

Shemesh N, Alvarez GA, Frydman L. Measuring small compartment dimensions by probing diffusion dynamics via Non-uniform Oscillating-Gradient Spin-Echo (NOGSE) NMR. J Magn Reson. 2013; 237:49–62. [PubMed: 24140623]

Sled JG, Pike GB. Quantitative interpretation of magnetization transfer in spoiled gradient echo MRI sequences. J Magn Reson. 2000; 145:24–36. [PubMed: 10873494]

Smith SA, Edden RAE, Farrell JAD, Barker PB, Van Zijl PCM. Measurement of T1 and T2 in the cervical spinal cord at 3 tesla. Magn Reson Med. 2008; 60:213–219. [PubMed: 18581383]

Song S-K, Yoshino J, Le TQ, Lin SJ, Sun S-W, Cross AH, Armstrong RC. Demyelination increases radial diffusivity in corpus callosum of mouse brain. Neuroimage. 2005; 26:132–140. [PubMed: 15862213]

Standring S. Gray's anatomy. The anatomical basis of clinical practice. 2008

Standring S, Ellis H, Healy JC. Gray's anatomy: the anatomical basis of clinical practice. American Journal. 2005

Stejskal EO, Tanner JE. Spin Diffusion Measurements: Spin Echoes in the Presence of a Time-Dependent Field Gradient. J Chem Phys. 1965; 42:288–292.

Stepišnik J. Time-dependent self-diffusion by NMR spin-echo. Physica B Condens Matter. 1993; 183:343–350.

Stikov N, Perry LM, Mezer A, Rykhlevskaia E, Wandell BA, Pauly JM, Dougherty RF. Bound pool fractions complement diffusion measures to describe white matter micro and macrostructure. Neuroimage. 2011; 54:1112–1121. [PubMed: 20828622]

Summers P, Staempfli P, Jaermann T, Kwiecinski S, Kollias S. A preliminary study of the effects of trigger timing on diffusion tensor imaging of the human spinal cord. AJNR Am J Neuroradiol. 2006; 27:1952–1961. [PubMed: 17032874]

Trobe JD. The Human Brain. An Introduction to Its Functional Anatomy. J Neuroophthalmol (6th). 2010; 30:107.

Walsh DO, Gmitro AF, Marcellin MW. Adaptive reconstruction of phased array MR imagery. Magn Reson Med. 2000; 43:682–690. [PubMed: 10800033]

Wang LZ, Caprihan A, Fukushima E. The Narrow-Pulse Criterion for Pulsed-Gradient Spin-Echo Diffusion Measurements. J Magn Reson A. 1995; 117:209–219.

Waxman, SG.; Kocsis, JD.; Stys, PK. The Axon: Structure, Function, and Pathophysiology. Oxford University Press; 1995.

Wheeler-Kingshott CAM, Cercignani M. About “axial” and “radial” diffusivities. Magn Reson Med. 2009; 61:1255–1260. [PubMed: 19253405]

Whittall KP, MacKay AL, Graeb DA, Nugent RA, Li DK, Paty DW. In vivo measurement of T2 distributions and water contents in normal human brain. Magn Reson Med. 1997; 37:34–43. [PubMed: 8978630]

Zhang H, Hubbard PL, Parker GJM, Alexander DC. Axon diameter mapping in the presence of orientation dispersion with diffusion MRI. Neuroimage. 2011; 56:1301–1315. [PubMed: 21316474]

Highlights

- In vivo mapping of axon diameter in the human spinal cord at 300 mT/m
- Atlas-based analysis that takes into account partial volume effect
- Axon diameters ranged from 3.0 μm (gracilis) to 5.9 μm (spinocerebellar tract).

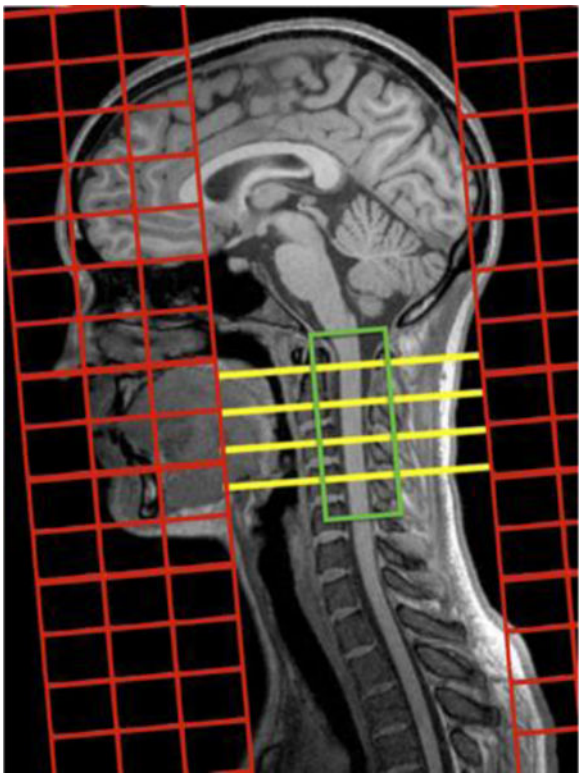

Figure 1.

Placement of slices (yellow), saturation bands (red) and shimming volume (green). Four slices were placed in the middle of the vertebral body at levels C1, C2, C3 and C4, by adjusting the slice gap for each subject. Slices were orthogonal to the SC. Optimal shim coefficients (up to 2nd order) were calculated within a small box encompassing the spinal cord. To prevent aliasing associated with reduced FOV, two saturation bands were prescribed anteriorly and posteriorly.

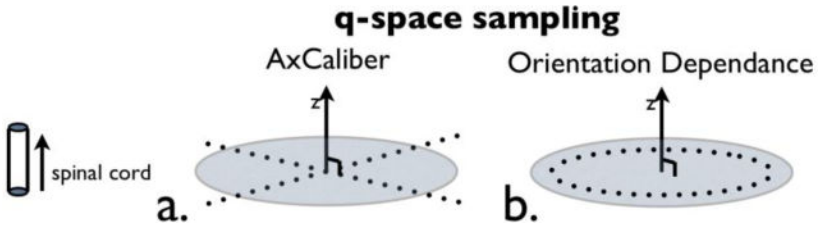

Figure 2.

Illustration of the diffusion encoding gradients used in the AxCaliber protocol (a) and in the protocol for probing orientation dependence (b). The latter protocol aims at exploring fibers that are not oriented along Z (e.g., collateral fibers entering the dorsal aspect of the cord).

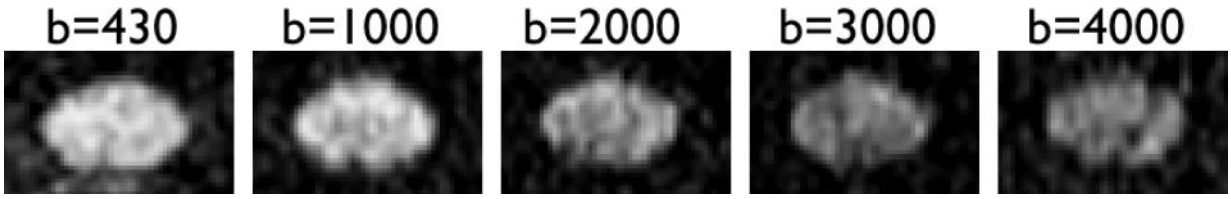

Figure 3.

Examples of DW images with selected b-values in the lowest range (430<b<4000 s/mm^2) used for motion correction. These images offer sufficient SNR for robust estimation of motion parameters without CSF contamination.

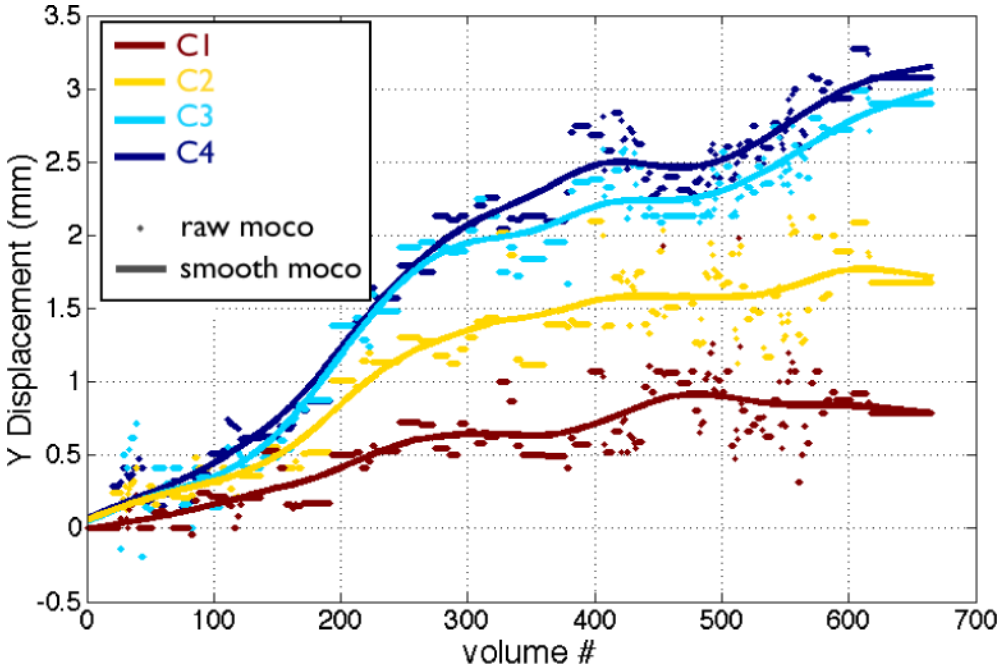

Figure 4.

Estimated motion in anteroposterior direction (raw moco) and fitted spline functions (smooth moco) at each cervical level in one subject. All data with different Δ were concatenated. Here, “moco” stands for motion correction.

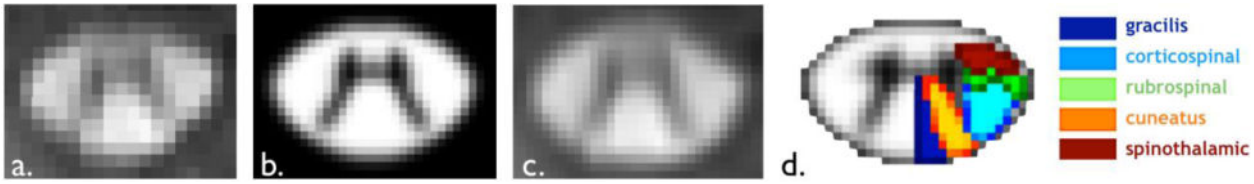

Figure 5.

a: Mean high b-values images. b: image of the template used for registration. c: registered image after applying the deformation field. d: Five major axonal pathways with different morphological features were selected from the white matter atlas in order to extract model-based diffusion MRI metrics.

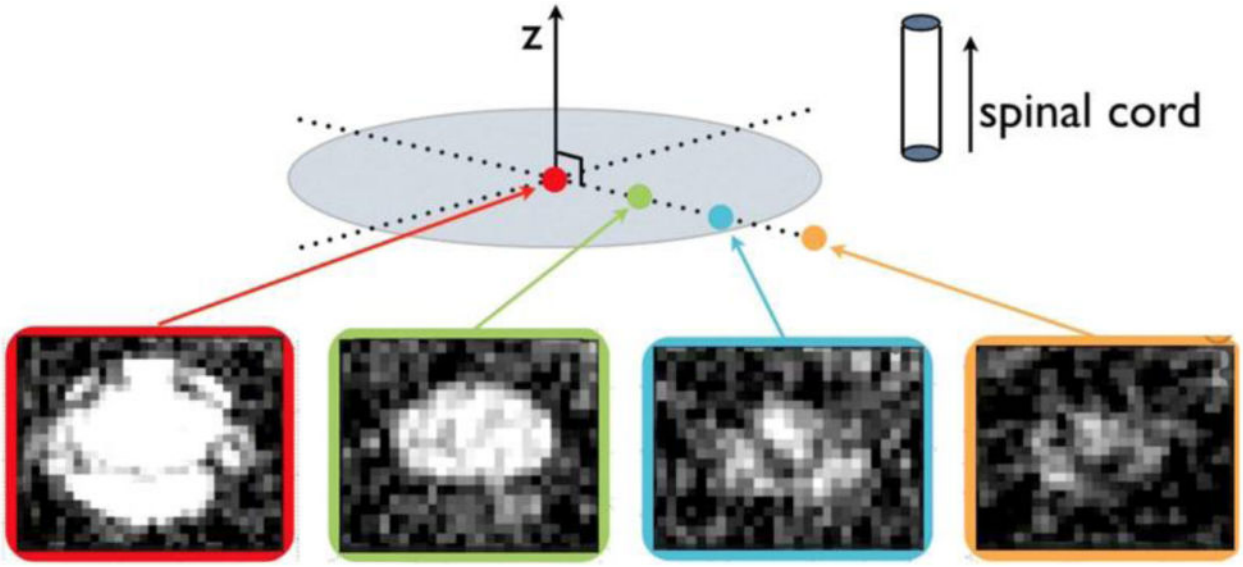

Figure 6.

Example of images acquired at different q-vectors. Data are not interpolated. Contrast is kept the same for better comparison. Notice the low SNR at very-high q-value (orange), which was compensated by averaging over the four directions.

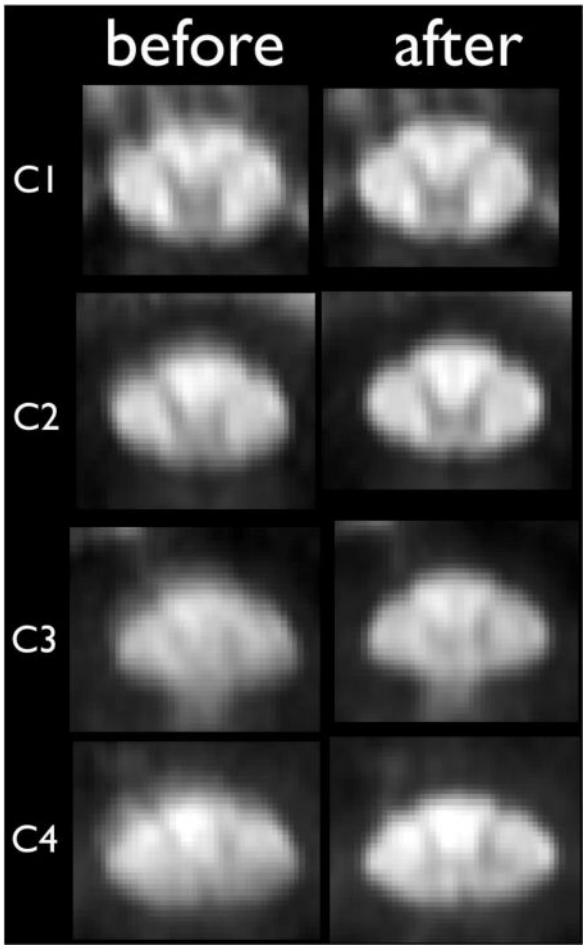

Figure 7.
Data averaged along q-values in one subject (excluding images acquired at b < 430s/mm^2), before and after applying the correction for eddy-currents and subject motion.

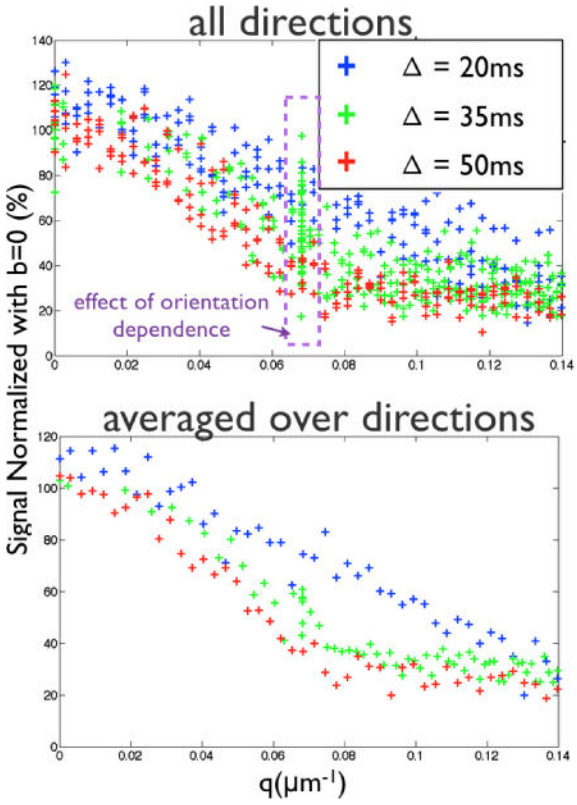

Figure 8.

Top: Rician corrected q-space data in one voxel of the spinal cord white matter for one subject before LPCA correction (normalized by b=0). Bottom: same data averaged over the four directions. The purple dashed box shows the data collected for probing the orientation dependence (see Figure 2.b.).

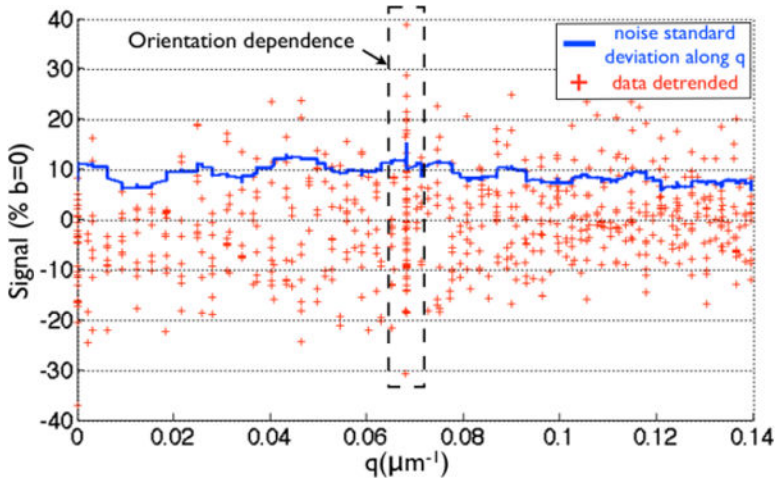

Figure 9.

Standard deviation of noise along q (blue curve) in one voxel and one subject before LPCA correction. Values are shown as percentage of the b=0 signal. This estimated noise includes thermal and physiological noise. Notice that the standard deviation is fairly constant along q.

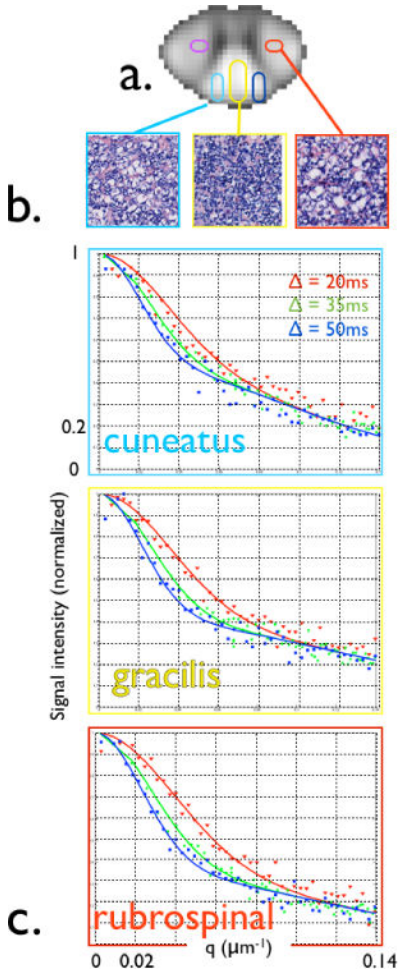

Figure 10.

a: Cuneatus (blue), gracilis (yellow) and rubrospinal (red) tracts highlighted on the mean DWI in one subject. b. Histological images of axons stained for myelin (luxol fast blue cross) over corresponding pathways of a human spinal cord ("Histology at the University of Michigan," n.d.), reproduced with permission. c. Model fitting on signal decay acquired in one subject on a single voxel in the corresponding regions.

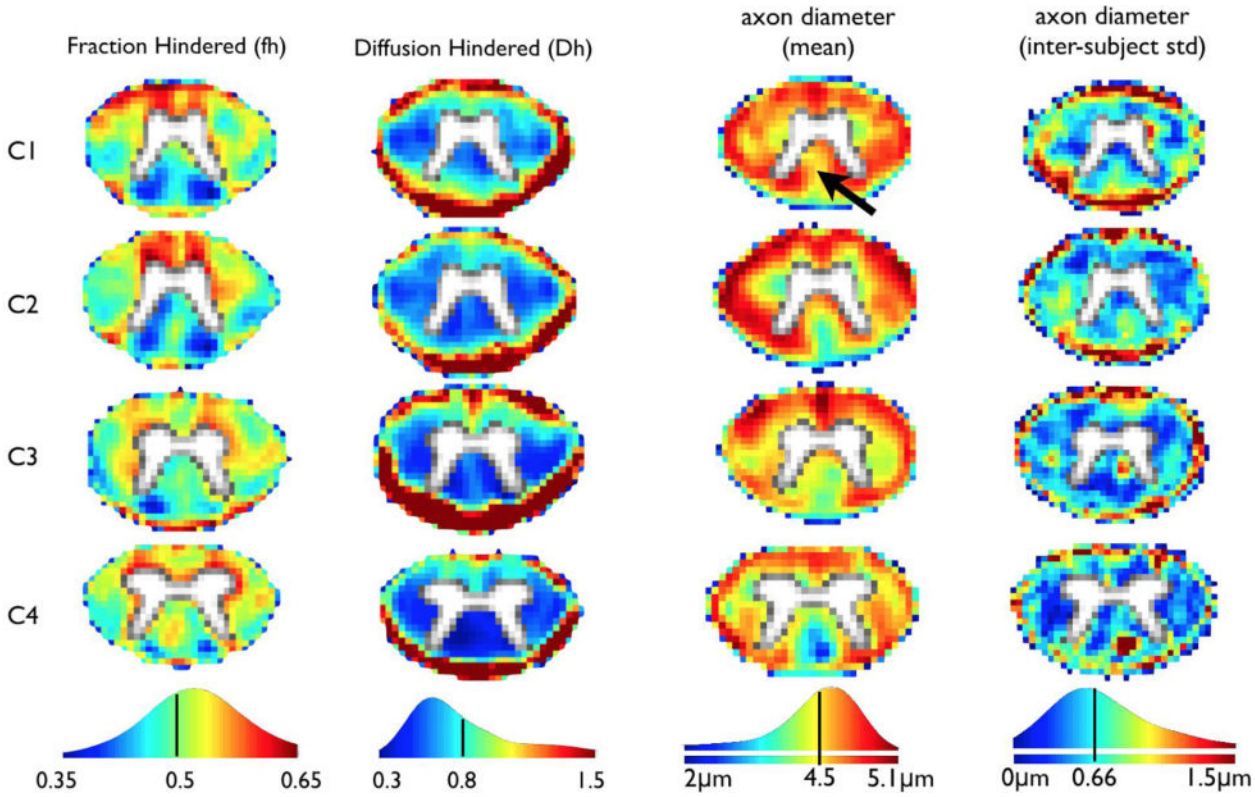

Figure 11.

Maps of fitted parameters using single diameter model. Data histograms with range and mean value are shown at the bottom. The black arrows points to the posterior funiculus,

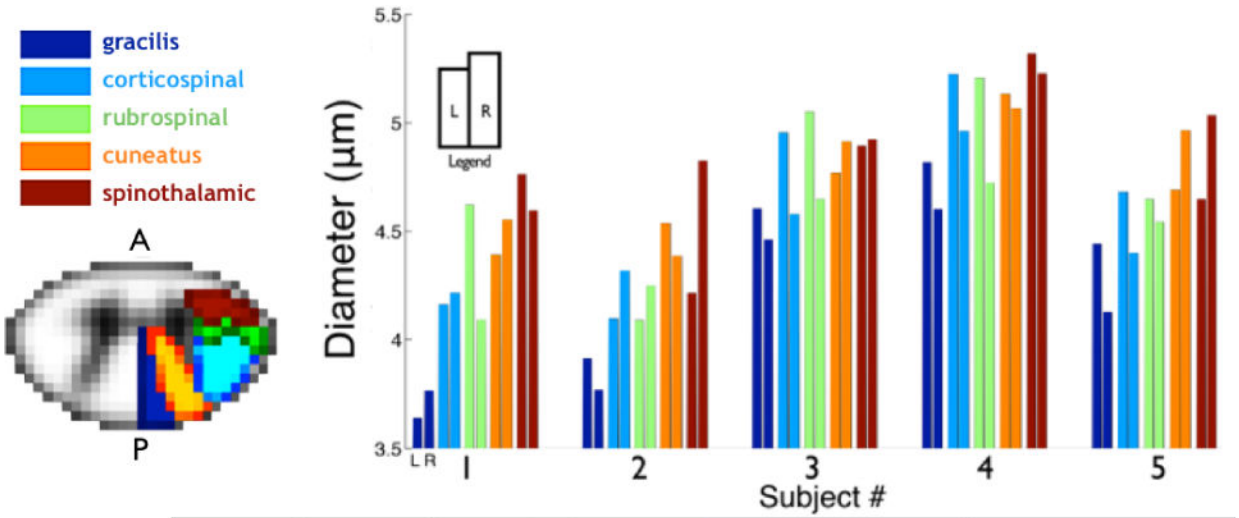

	Mean axon diameter (µm)				fh			
	right	left	mean	std across subjects	right	left	mean	std across subjects
gracilis	3.55	3.47	**3.51**	0.54	0.49	0.49	**0.49**	0.01
cuneatus	4.15	4.16	**4.15**	0.46	0.45	0.45	**0.45**	0.02
corticospinal	4.17	4.10	**4.14**	0.48	0.53	0.52	**0.52**	0.02
rubrospinal	3.81	4.03	**3.92**	0.35	0.56	0.51	**0.54**	0.01
spinothalamic	3.69	3.74	**3.71**	0.36	0.57	0.55	**0.56**	0.01

	Dh (µm²/ms)			
	right	left	mean	std across subjects
gracilis	1.01	1.06	**1.04**	0.21
cuneatus	0.75	0.85	**0.80**	0.24
corticospinal	0.66	0.77	**0.72**	0.18
rubrospinal	0.52	0.72	**0.62**	0.10
spinothalamic	0.60	0.57	**0.58**	0.07

Three-way ANOVA test

parameter:	Laterality	Subject	Pathway
p-value:	0.244	3.42E-8	3.54E-6

Figure 12.

Top left: Mean DWI with overlay of ROIs for computing parameters within specific white matter tracts. Top right: Bar graph showing estimated axon diameter within tracts, laterality and subject. The estimated axon diameters range between 3.5 and 5.5*µm*, suggesting fairly precise estimate of axon diameters on an individual basis. Bottom table: Estimated parameters averaged across subjects. Mean axon diameter was 3.51 (+/−0.54), 4.15 (+/−0.46) and 3.71 (+/− 0.36) µm in the gracilis, cuneatus and spinothalamic tracts, respectively. The restricted water fraction (1-fh), which correlates with axon density, was 55% and 44% (+/− 2%) in the cuneatus and spinothalamic tracts, respectively. Results of the three-way ANOVA show a significant effect of pathway and subjects but no effect for laterality.

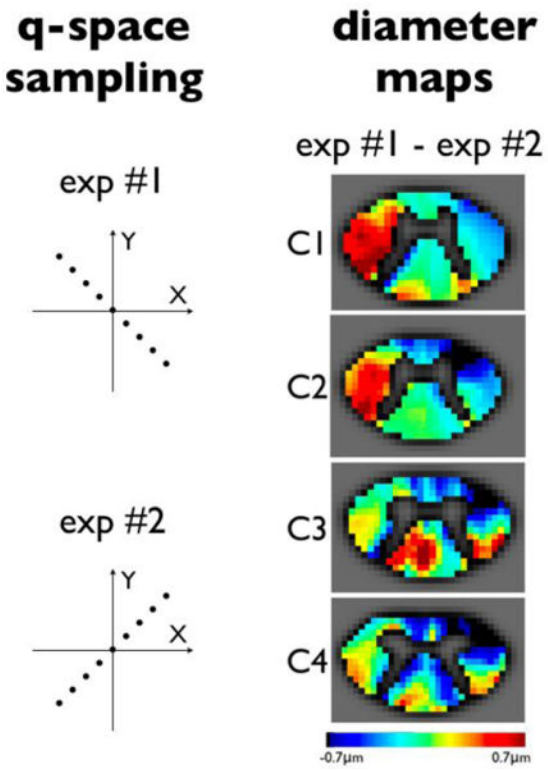

Figure 13.

Difference in axon diameter estimated using two sub-sets of data with orthogonal diffusion gradient direction (X,Y;−X, −Y) and (−X,Y; X, −Y) in one subject. Symmetrical differences (red versus blue) are observed in the lateral region (especially at C1 and C2), which could be attributed to the presence of collateral fibers.

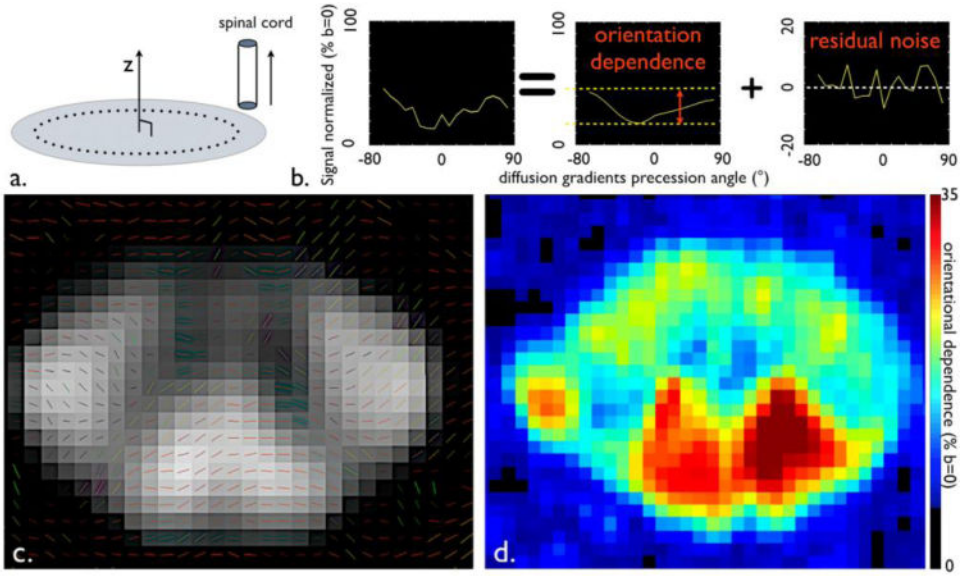

Figure 14.

a. q-space sampling for orientation dependence study. b. Signal at different gradient orientations, which was detrended using cosines into a function representing the signal variation as a function of gradient orientation ("orientation dependence" plot). c. Directions of collateral fibers averaged across subjects at level C2. This map was obtained by extracting the angular value corresponding to the highest diffusion (i.e. lower signal). d: Corresponding map of orientation dependence obtained using the peak-to-peak amplitude from the orientation dependence plot.

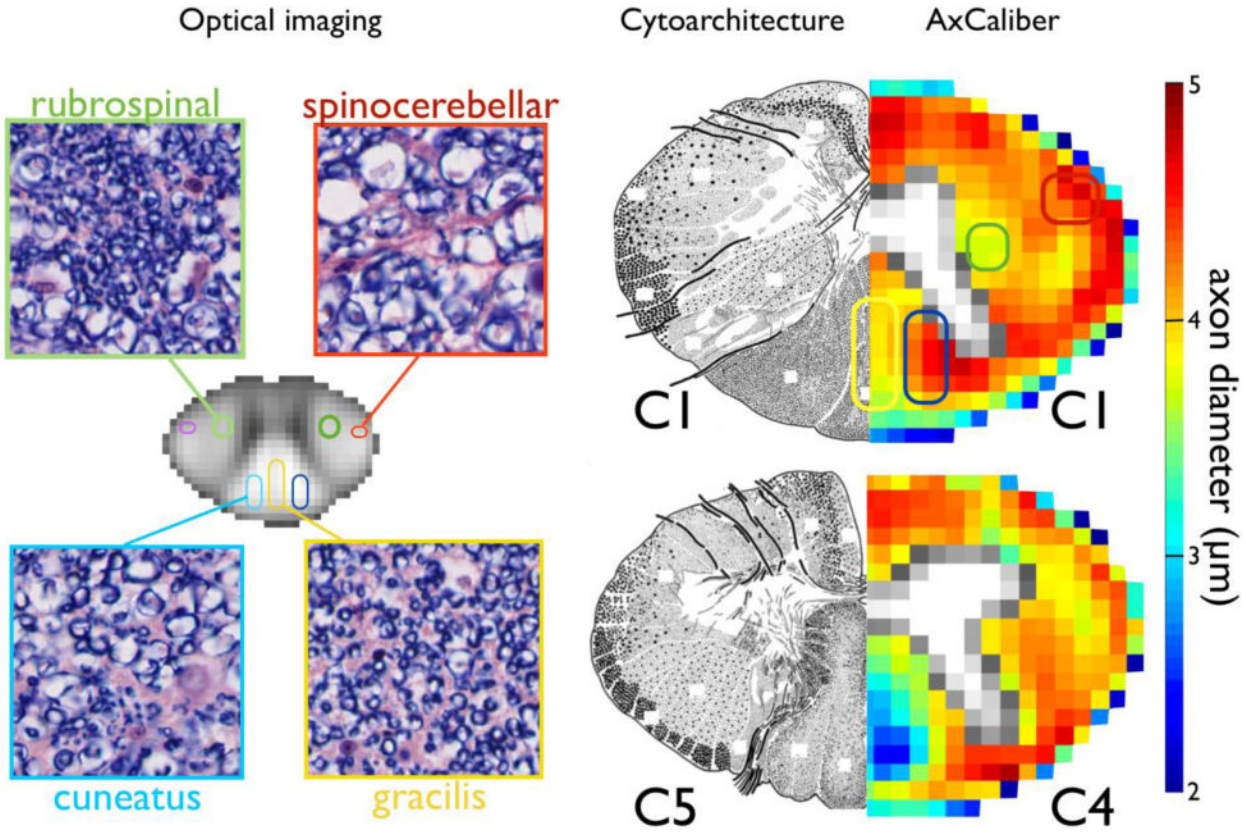

Figure 15.

Comparison of AxCaliber results with two histological resources. Left: Optical images ($50\times50\mu m^2$) of human thoracic spinal cord ("Histology at the University of Michigan," n.d.), reproduced with permission. Middle: Cytoarchitecture of human spinal cord white matter at vertebral levels C1 and C5 (Nieuwenhuys et al., 2007), reproduced with permission. Axon size is gray-level coded (the darker the bigger). Note that this representation of axon diameter is qualitative. Notice that some tracts have monodisperse axonal sizes (e.g. spinocerebellar and gracilis), while others present some super-axons surrounded by tiny axons (e.g. Pyramidal tracts). For direct comparison, AxCaliber results (averaged over five subjects) are overlaid on the right portion of the cytoarchitecture map at the corresponding levels (note: given that we did not acquire lower than C4, the C4 level is shown next to the C5 level from the cytoarchitecture map). Regions corresponding to the optical imaging panel are circled on the AxCaliber maps: gracilis (yellow), cuneatus (blue), rubrospinal (green) and spinocerebellar (red).

Table 1

SNR computed per subject and per vertebral level at b=0 and b=39,011 s/mm^2 (b_{max})

	Subject #1		Subject #2		Subject #3		Subject #4		Subject #5	
Z	**SNR b_{max}**	**SNR b_0**	**SNR b_{max}**	**SNR b_0**	**SNR b_{max}**	**SNR b_0**	**SNR b_{max}**	**SNR b_0**	**SNR b_{max}**	**SNR b_0**
C1	1.8	8.6	1.7	8.1	2.2	12.7	1.9	12.2	1.1	9.1
C2	1.7	8.1	1.6	8.5	1.9	11.5	1.6	10.8	1.5	10.5
C3	1.8	10.0	1.9	9.1	2.0	11.6	1.5	11.2	1.5	11.3
C4	1.7	9.1	1.6	8.9	2.1	10.9	1.3	9.6	1.5	10.4
Average	1.8	9.0	1.7	8.7	2.1	11.7	1.6	11.0	1.4	10.3

Table 2

Goodness of fits using χ^2_{red} statistics. α represents the probability that our data are well described with the AxCaliber model (the higher the better).

Subject #	**1**	**2**	**3**	**4**	**5**
χ_{red}^2	1.23	1.21	1.09	1.15	1.18
α	5E-5	2E-4	5E-2	5E-3	1E-3